A Flexure-Based Kinematically Decoupled Micropositioning Stage with a Centimeter Range Dedicated to Micro/nano Manufacturing

Fujun Wang, Cunman Liang, Yanling Tian, *Member*, *IEEE*, Xingyu Zhao, and Dawei Zhang

***Abstract*—Precision positioning stages with large strokes and high positioning accuracy are attractive for high-performance micro/nano manufacturing. This paper presents the dynamic design and characteristic investigation of a novel XY micropositioning stage. Firstly, the mechanism of the stage was introduced. The XY stage was directly driven by two linear motors, and the X- and Y- axes kinematic decoupling was realized through a novel flexible decoupling mechanism based on flexure hinges and preloaded spring. The dynamic model of the XY stage was established, and the influences of the rotational stiffness of the flexure hinge and the initial positions of the working table on the dynamic rotation of the positioning stage were investigated. The stiffness and geometric parameters of the flexure hinges were determined at the condition that the angular displacements of the working table were within ±0.5° with a motion stroke of ±25 mm. Finally the stage performance was investigated through simulation and experiments, the X- and Y-axes step responses, the rotation angular and positioning accuracy of the stage were obtained. The results show that the stage exhibits good performance and can be used for micro/nano manufacturing.**

***Index Terms*—Positioning stages, Linear motors, Direct-drive, Kinematic decoupling, Dynamic design**

I. Introduction

High speed precision positioning stages play an important role in micro/nano academic research and industrial manufacturing, where a micro/nanometer-scale resolution with motion strokes over tens of millimeters is a big challenge for the applications such as microelectronicmechanical and biomedical device manufacturing [1]-[5].

Recently, the design and control of high speed XY precision positioning stages have been received considerable attentions from researchers [6]-[8]. Because of the large deformation and good position recovery ability, shape memory alloy (SMA) actuators were adopted to ensure the fast responses of the positioning systems [9], [10]. Liang et al. studied on the SMA actuator modeling to improve the performance of SMA actuated positioning systems [11]. Riccardi et al. presented the configuration and control of a SMA actuated precision positioning system with a tracking error of 2 μm [12]. The SMA actuated system can provide appropriate performance. However, the accuracy of the SMA actuated systems is limited due to the high hysteretic behavior of SMA actuators [13]. PZT actuators have been widely used in micro/nano positioning system due to their advantages of large pushing force, nanometer-scale motion resolution and fast response [14]-[17]. Yao et al. proposed a novel PZT actuated parallel-kinematic mechanisms for integrated, multi-axis nanopositioning [18]. Qin et al. presented the mechanism design of a decoupled PZT actuated positioning stage [19]. Gu et al. studied the motion control of a piezoelectric positioning stage [20]. Nanometer-scale positioning accuracy can be achieved through PZT actuation. However, the PZT actuators generally generate small motion displacements, making it not suitable to actuate a precision positioning stage targeted for a motion stroke over tens of millimeters [21]-[23].

Electromagnetic actuation is considered to be a good choice for the motion with a stroke of over several millimeters. Linear motors have advantages of fast response, smooth output force and no stroke limit [24]. As a result, this paper presents the dynamic design of a linear motor driven stage to obtain a large stroke and sub-micrometer positioning accuracy. To achieve high speed, a flexible decoupling mechanism is designed.

The rest of the paper is organized as follows: Section II introduces the mechanism of the XY micropositioning stage. In section III, the dynamic modeling of the stage is carried out. Then the dynamic design and analysis are finished in section IV. After that the experiments are presented in Section V to investigate the performance of the developed micropositioning stage. Finally, Section VI concludes this paper.

II. Mechanism of the XY positioning stage

Figure 1 illustrates the mechanism of the XY positioning stage composed of the base, X- and Y-axes linear motors,

Manuscript received on March 22, 2015. This work was supported in part by the National Natural Science Foundation of China under Grant nos 51205279, 51275337 and 51175372, in part by the Science & Technology Commission of Tianjin Municipality under Grant nos 13JCQNJC04100 and 15JCYBJC19600, the Tianjin University for Peiyang Elite Scholar under Grant no. 60301014, Open Project of Tianjin Key Laboratory of Equipment Design and Manufacturing Technology and key Laboratory of Mechanism Theory and Equipment Design of Ministry of Education.

F. J. Wang, C. M. Liang, Y. L. Tian, X. Y. Zhao, and D. W. Zhang are with Tianjin Key Laboratory of Equipment Design and Manufacturing Technology, School of Mechanical Engineering, Tianjin University, Tianjin 300072, China (email: wangfujun@tju.edu.cn, lcm@tju.edu.cn, meytian@tju.edu.cn, zxytju@tju.edu.cn, medzhang@tju.edu.cn,)

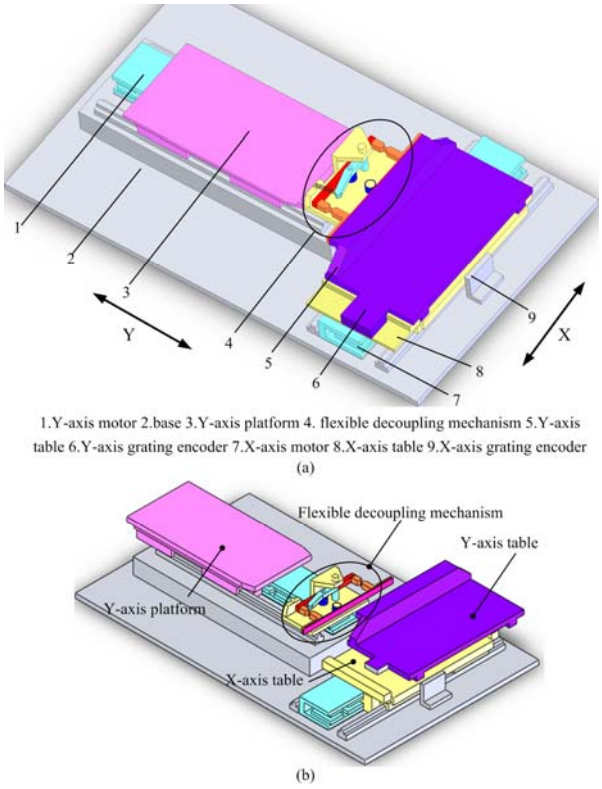

Fig.1. XY positioning stage: (a) overall mechanism and (b) explosion view.

X- and Y-axes tables (the working table), the flexible decoupling mechanism, X- and Y-axes linear grating encoders and Y-axis motion platform. Both of the X- and Y-axes linear motors are fixed on the base. Y-axis platform is connected with the rotor of Y-axis linear motor by bolts. X-axis table is connected with the rotor of X-axis linear motor. As shown in Fig.1(b), Y-axis table is located above X-axis table, and it is also connected with Y-axis platform through the flexible decoupling mechanism. X-axis readhead system of the grating encoder is installed on the base, and the grating scale of the grating encoder is mounted on the side face of X-axis table. Y-axis readhead system of the grating encoder is fixed on Y-axis table, and the grating scale of the grating encoder is mounted on the side face of Y-axis table.

The XY stage is directly driven by two linear motors, a novel flexible decoupling mechanism is designed between the Y-axis platform and the Y-axis table, so that the X- and Y-axes linear motors can be both fixed on the base and the mass and inertia of the motion parts of the XY stage are significantly reduced.

Figure 2(a) shows the flexible decoupling mechanism consisting of the guiding fin, front and back roller bearings, flexure hinges, front and back lapping plates, preloaded connecting rod, front and back shaft, and the preloaded spring. The guiding fin is fixed on the Y-axis platform, and the front lapping plate is fixed on Y-axis table. The preload spring is used to eliminate the clearance between front roller bearing and front lapping plate. X-and Y-axes tables have no relative motion along X axis. Because of the existence of the decoupling mechanism, Y-axis table can move along X axis together with X-axis table.

Figure 2(b) shows the schematic diagram of the decoupling principle, where F_x and F_y are the output forces of X- and Y-axes motors, respectively. F_1 is the normal force between the back roller bearing and the back lapping plate. F_2 is the normal force between the front roller bearing and the front lapping plate. f_1 is the friction force between the back roller bearing and the back lapping plate. f_2 is the friction force between the front roller bearing and the front lapping plate. F is the preload force of the preload spring. The Y-axis motor generates a force F_y, which will drive the Y-axis table by the flexible decoupling mechanism. When X-axis motor generates a force F_x, the Y-axis table will move with X-axis table in X direction, the front and back roller bearings roll along the front and back lapping plate separately, and thus the motion decoupling of X -and Y-axes is realized.

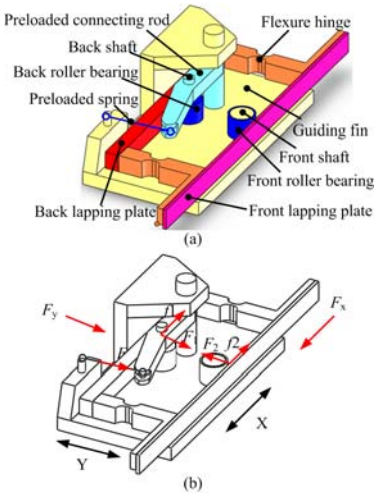

Fig.2. The flexible decoupling mechanism: (a) mechanism and (b) decoupling principle.

III. DYNAMIC MODELING OF THE XY POSITIONING STAGE

A. *Y-axis dynamic translation model*

Y-axis mechanical system of the positioning stage can be equivalent to a lumped mass spring system as shown in Fig.3(a), where k_t is the equivalent stiffness of the flexure hinge, k is the stiffness of the preloaded spring, k_c is the contact stiffness between the roller bearing and the lapping plate, M_{yd}, M_{y1}, M_{yh}, M_{y2} and M_{y3} are the masses of the rotor of Y-axis linear motor, platform, guiding fin, back lapping plate and table, respectively, k_{y1} and c_{y1} are the equivalent stiffness and damping coefficient of the bolt connections between the rotor of linear motor and the platform, respectively, k_{y2} and c_{y2} are the stiffness and damping coefficient of the bolted connections between the platform and guiding fin, respectively, k_g is the electromagnetic stiffness of the linear motor, c_{y3} is the damping coefficient between front roller bearing and front lapping plate, c_{y4} is the equivalent damping coefficient between back roller bearing

and back lapping plate, μ_{y1} is the friction coefficient between the platform and the slider, μ_{y2} is the friction coefficient between the Y-axis table and the slider, y_1, y_2, y_3, y_4 and y_5 are the Y-axis displacements of the rotor of Y-axis linear motor, platform, guiding fin, back lapping plate and table, respectively, U_y is the driving voltage of Y-axis linear motor, R is the equivalent resistance of the linear motor coil, L is the inductor of the motor coil, and i_y is the current intensity through the coil.

The relationship between U_y and I_y can be expressed as

$$i_y R + L\frac{di_y}{dt} + k_e\frac{dy_1}{dt} = U_y \tag{1}$$

where k_e is back electromotive force constant.

The relation between the output force and the input current of the Y-axis linear motor can be expressed as

$$F_y = k_b i_y \tag{2}$$

where k_b is force constant of the linear motor.

The dynamics of the Y-axis motor-table servomechanism are represented by the following differential equations:

$$M_{yd}\frac{d^2y_1}{dt^2} + c_{y1}\frac{dy_1}{dt} - c_{y1}\frac{dy_2}{dt} + (k_g + k_{y1})y_1 - k_{y1}y_2 = F_y \tag{3}$$

$$\begin{aligned} &M_{y1}\frac{d^2y_2}{dt^2} - c_{y1}\frac{dy_1}{dt} + (c_{y1} + c_{y2} + u_{y1})\frac{dy_2}{dt} \\ &\quad - c_{y2}\frac{dy_3}{dt} - k_{y1}y_1 + (k_{y1} + k_{y2})y_2 - k_{y2}y_3 = 0 \end{aligned} \tag{4}$$

$$\begin{aligned} &M_{yh}\frac{d^2y_3}{dt^2} - c_{y2}\frac{dy_2}{dt} + (c_{y2} + c_{y3} + c_{y4})\frac{dy_3}{dt} - c_{y3}\frac{dy_4}{dt} \\ &\quad - c_{y4}\frac{dy_5}{dt} - k_{y2}y_2 + (k_{y2} + k_{eq} + k_c)y_3 - k_{eq}y_4 - k_c y_5 = 0 \end{aligned} \tag{5}$$

$$M_{y2}\frac{d^2y_4}{dt^2} - c_{y3}\frac{dy_3}{dt} + c_{y3}\frac{dy_4}{dt} - k_{eq}y_3 + (k_{eq} + 2k_t)y_4 - 2k_k y_5 = 0 \tag{6}$$

$$M_{y3}\frac{d^2y_5}{dt^2} - c_{y4}\frac{dy_3}{dt} + (c_{y4} + u_{y2})\frac{dy_5}{dt} - k_c y_3 - 2k_t y_4 + (k_c + 2k_t)y_5 = 0 \tag{7}$$

where $k_{eq} = \dfrac{k_c k}{k + k_c}$.

B. X-axis dynamic translation model

X-axis system is equivalent to a lumped mass spring system shown in Fig.3(b), where M_{xd}, M_{x1} and M_{x2} are the masses of the rotor of X-axis linear motor, X-axis table and Y-axis table, respectively, k_{x1} and c_{x1} are the equivalent stiffness and damping coefficient of the bolt connections between the rotor of linear motor and X-axis table, respectively, k_{x2} and c_{x2} are

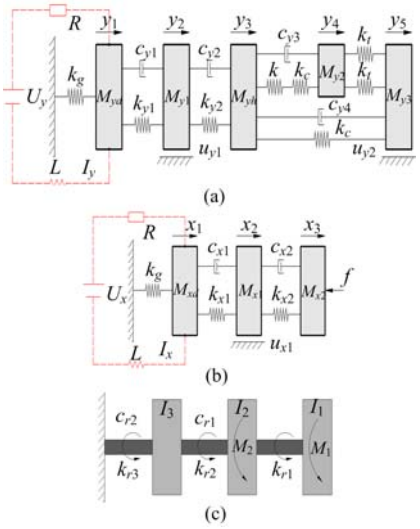

Fig.3. Dynamic model of the servomechanical system: (a) Y-axis translation, (b) X-axis translation and (c) Z-axis rotation.

equivalent contact stiffness and damping coefficient of the cross roller guide between X- and Y-axes tables, respectively, μ_{y1} is the friction coefficient between the X-axis table and the slider, x_1, x_2 and x_3 are the displacements of the rotor of X-axis linear motor, X-axis table and Y-axis table, respectively, U_x is the driving voltage of X-axis linear motor, and i_x is the current intensity through the coil.

The relationship between U_x and i_x can be expressed as

$$i_x R + L\frac{di_x}{dt} + k_e\frac{dx_1}{dt} = U_x \tag{8}$$

The relation between the output force and the input current of the X-axis linear motor can be expressed as

$$F_x = k_b i_x \tag{9}$$

The dynamics of the X-axis motor-table servomechanism are represented by the following differential equations:

$$M_{xd}\frac{d^2x_1}{dt^2} + c_{x1}\frac{dx_1}{dt} - c_{x1}\frac{dx_2}{dt} + (k_g + k_{x1})x_1 - k_{x1}x_2 = k_b i_x \tag{10}$$

$$\begin{aligned} &M_{x1}\frac{d^2x_2}{dt^2} - c_{x1}\frac{dx_1}{dt} + (c_{x1} + c_{x2} + u_{x2})\frac{dx_2}{dt} \\ &\quad - c_{x2}\frac{dx_3}{dt} - k_{x1}x_1 + (k_{x1} + k_{x2})x_2 - k_{x2}x_3 = 0 \end{aligned} \tag{11}$$

$$M_{x2}\frac{d^2x_3}{dt^2} - c_{x2}\frac{dx_2}{dt} + c_{x2}\frac{dx_3}{dt} - k_{x2}x_2 + k_{x2}x_3 = f \tag{12}$$

where f is the friction of front and back roller bearings to Y-axis table, and it is affected by the Y-axis dynamic load.

The following equations can be obtained:

$$F_1 = k_{eq}(y_3 - y_4) + c_{y3}(\frac{dy_3}{dt} - \frac{dy_4}{dt}) - F_{pre} \quad (13)$$

$$f_1 = -sign(\frac{dx_3}{dt})u_{x2}F_1 \quad (14)$$

$$F_2 = k_c(y_3 - y_5) + c_{y4}(\frac{dy_3}{dt} - \frac{dy_5}{dt}) + F_{pre} \quad (15)$$

$$f_2 = -sign(\frac{dx_3}{dt})u_{x2}F_2 \quad (16)$$

$$f = f_1 + f_2 \quad (17)$$

where F_{pre} is the normal force that front and back roller bearings apply to the front and back lapping plates with only the preload spring working. Since the back roller bearing is in the middle of the preloaded connecting rod, F_{pre}=2F.

C. Dynamic rotation along Z-axis

When X- and Y-axes tables move at the same time, Y-axis dynamic load will deviate from the rotation center of Y-axis table. In addition, the frictions f_1 and f_2 also deviate from the rotation center of the Y-axis table. The working table will rotate about Z-axis, affecting the positioning accuracy of the XY stage. Thus, it is necessary to investigate the dynamic rotation of the working table along Z-axis.

Figure 3(c) shows the dynamic rotation model of the XY stage along Z-axis, where I_1, I_2 and I_3 are the moments of inertia of the back lapping plate, working table and X-axis table, respectively, k_{r1} is the equivalent rotational stiffness of the flexure hinge, k_{r2} and c_{r1} are the equivalent rotational stiffness and damping coefficient between X-axis table and working table, respectively, k_{r3} and c_{r2} are the equivalent rotational stiffness and angle damping coefficient between X-axis table and the base, respectively, M_1 is the moment applied to the back lapping plate, and M_2 is the moment applied to working table.

The dynamic rotation along Z-axis of the XY stage can be expressed as

$$I_1\frac{d^2\varphi_1}{dt^2} + k_{r1}\varphi_1 - k_{r1}\varphi_2 = M_1 \quad (18)$$

$$I_2\frac{d^2\varphi_2}{dt^2} + c_{r1}\frac{d\varphi_2}{dt} - c_{r1}\frac{d\varphi_3}{dt} - k_{r1}\varphi_1 + (k_{r1} + k_{r2})\varphi_2 - k_{r2}\varphi_3 = M_2 \quad (19)$$

$$I_3\frac{d^2\varphi_3}{dt^2} - c_{r1}\frac{d\varphi_2}{dt} + (c_{r1} + c_{r2})\frac{d\varphi_3}{dt} - k_{r2}\varphi_2 + (k_{r2} + k_{r3})\varphi_3 = 0 \quad (20)$$

where φ_1, φ_2, φ_3 are the angular displacements of the back lapping plate, working table and X-axis table, respectively, k_r is the rotational stiffness of the flexure hinge, $k_{r1} = 2k_r$, $M_1 = F_1x_3 - f_1l_1$, and $M_2 = -F_2x_3 - f_2l_2$.

The schematic diagram of the stiffness and damping of the slider is shown in Fig.4.

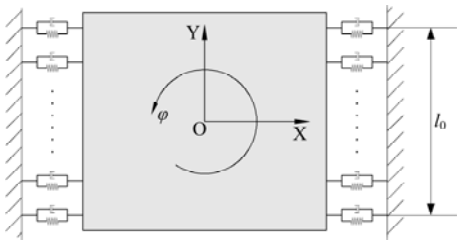

Fig.4. The schematic diagram of the stiffness and damping of the slider.

If there are 2n spring-damper units on each slider between the table and the slider, the equivalent rotational stiffness and damping coefficient can be calculated as

$$k_{req} = \frac{l_0^2}{n}k_{cn}\sum_{k=1}^{n}(\frac{2k-1}{2(2n-1)})^2 \quad (21)$$

$$c_{req} = \frac{l_0^2}{n}c_{cn}\sum_{k=1}^{n}(\frac{2k-1}{2(2n-1)})^2 \quad (22)$$

where K_{cn} and c_{cn} are equivalent contact stiffness and damping coefficient, respectively.

If there are (2n+1) spring-damper units on each slider between the table and the slider, the equivalent rotational stiffness and damping can be obtained as

$$k_{req} = \frac{l_0^2}{2(2n+1)}k_{cn}\sum_{k=1}^{n}(\frac{k}{2n})^2 \quad (23)$$

$$c_{req} = \frac{l_0^2}{2(2n+1)}c_{cn}\sum_{k=1}^{n}(\frac{k}{2n})^2 \quad (24)$$

Here, 10 (n=5) spring-damper units are adopted on each slider, and l_0=80 mm. The equivalent rotational stiffness and damping coefficient are obtained as

$$k_{r2} = 6.5185\times10^{-4}k_{x2},\ \ c_{r1} = 6.5185\times10^{-4}c_{x2} \quad (25)$$

$$k_{r3} = 6.5185\times10^{-4}k_{x3},\ \ c_{r2} = 6.5185\times10^{-4}c_{x3} \quad (26)$$

According to the working conditions and the motion characteristic parameter requirements, the liner motor can be selected and the dimensions of other components can be determined. The flexure hinges are the elastic components in the overall mechanism and have a great influence on the dynamic performance of the XY stage. The dynamic load and the residual vibrations during high speed motions and the instant interference generated when X- and Y-axes moves at the same time can be suppressed by the slight deformations of flexure hinges [25]. As a result, dynamic design is carried out considering the flexure hinge parameters.

Here circular-shaped flexure hinges are adopted. The structure and geometric parameters of the circular-shaped flexure hinge is shown in Fig.5(a).

The linear compliance of the flexure hinge along X-axis can be calculated as [25]

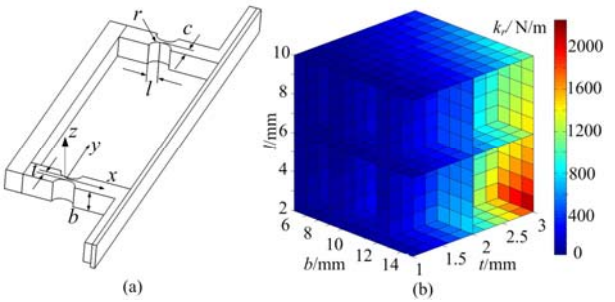

Fig. 5. Circular-shaped flexure hinge: (a) structure and (b) rotational stiffness.

$$\delta_t = \frac{1}{Eb}\left[\frac{2(1+\beta)}{\sqrt{2\beta+\beta^2}}\arctan\sqrt{\frac{2+\beta}{\beta}} - \theta + \cot\ln\frac{\beta(1+\gamma)}{\gamma(1+\beta)}\right] \tag{27}$$

where E is the Modulus of elasticity, $\gamma = t/2c$ and $\beta = t/2R$.

The X-axis linear stiffness $k_t = \frac{1}{\delta_t}$.

The rotational compliance of the flexure hinge along Z-axis can be calculated as

$$\delta_r = \frac{3}{2Ebr^2}\left\{\frac{1}{2\beta+\beta^2}\left[\frac{(3+2\beta+\beta^2)}{(2\beta+\beta^2)(1+\beta)} + \frac{6(1+\beta)}{(2\beta+\beta^2)^{3/2}}\arctan\sqrt{\frac{2+\beta}{\beta}}\right] + \frac{1}{(1+\beta)}\right\} \tag{28}$$

The Z-axis rotational stiffness $k_r = \frac{1}{\delta_r}$.

For circular-shaped flexure hinges, c=l=r. Figure 5(b) shows the rotational stiffness of the circular-shaped flexure hinge.

IV. Dynamic Design and Analysis

During frequent start-stop motions in X- and Y- axes, there will be dynamic rotations of the working table along Z-axis. The dynamic rotation of the working table is investigated and dynamic design is carried out to ensure the dynamic rotation angle of the working table is within 0.5° during motion process [26].

It is known from the dynamic rotation model that the rotational stiffness of the flexure hinge has a great effect on the dynamic rotation of the working table along Z-axis. Here the motion scope of the working table is defined as ±25mm. When the working table is at the limit position, the moment is the largest, and it is the most likely to rotate. The angular displacements of the back lapping plate and the working table when the working table is at the limit position are analyzed. Figure 6 (a) shows the maximum angular displacements of the working table with different angle stiffnesses of flexure hinges when the driving voltages in X- and Y-axes are both 20V and the working table is at the position of x_0=25mm. Figure 6 (b) shows the maximum angular displacements of working table with different angle stiffnesses of flexure hinges when the driving voltages in X- and Y-axes are both 20V and the working table is at the position of x_0=-25mm. Table 1 summarizes the parameters of the XY stage. The results show that the angle displacements of the back lapping plate and the working table decrease with the rotational stiffness increasing, and the maximum angle of the working table decreases rapidly firstly, and finally fluctuates within a certain range. To achieve good dynamic performance, the maximum angular displacement of the working table should remain within ±0.5°(8.7μrad). When the rotational stiffness k_r>180N/m, the maximum angular displacement of the working table remains less than ±0.5°.

The rotational stiffness of the flexure hinge is mainly determined by its geometric parameters. Figure 7 shows the rotational stiffness of the flexure hinge varying with t and l, where the red line represents that the rotational stiffness is 180 N/m. On the left of the line the rotational stiffness is less than 180 N/m, while on the right it is more than 180 N/m. Considering the dimensions of the XY stage, the geometric parameters are determined as l=c=r=4 mm and t=2 mm.

Figure 8 compares the angular displacements of the working table at different initial positions. The analysis results show that the angular displacements increase with the initial position of the working table increasing, and the angular displacement of working table is within ±0.5° with the motion stroke form -25mm to 25mm.

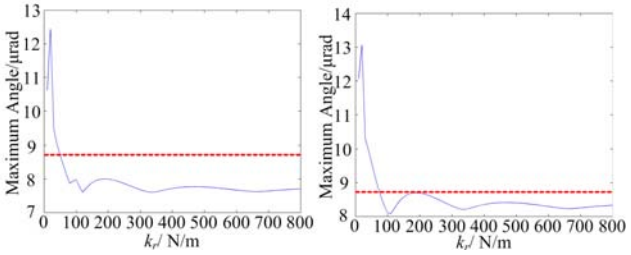

Fig.6. The maximum angular of the working table with different rotational stiffness of flexure at the position of (a) x_0=25mm and (b) x_0=-25mm.

TABLE I
THE PARAMETERS OF THE XY STAGE

M_{yd}(kg)	M_{y1}(kg)	M_{yh}(kg)	M_y(kg)	M_{y2}(kg)
1.03	1.5	1.2	0.1	1.6
u_{y1}(N·s/m)	u_{y2}(N·s/m)	k(N/m)	M_{xd}(kg)	M_{x1}(kg)
120	120	5×10^4	1.03	2.2
M_{x2}(kg)	c_{x1}(N·s/m)	c_{x2}(N·s/m)	I_1(kg·m^2)	I_2(kg·m^2)
1.6	800	800	0.0002	0.0098
I_3(kg·m^2)	E(Gpa)	b(m)	c(m)	F_{max}(N)
0.0098	206	0.01	0.004	176.2
c_{y1}(N·s/m)	c_{y2}(N·s/m)	c_{y3}(N·s/m)	c_{y4}(N·s/m)	k_{y1}(N/m)
800	800	800	800	2.6×10^5
k_{y2}(N/m)	k_c(N/m)	k_g(N/m)	k_{x1}(N/m)	k_{x2}(N/m)
2.6×10^5	4.03×10^5	7.5×10^5	2.6×10^5	2.6×10^5
u_{x1}(N·s/m)	u_{x2}(N·s/m)	l_1(m)	l_2(m)	t(m)
120	120	0.053	0.012	0.002
r(m)	L(H)	k_b(N/A)	R(Ω)	k_e(V·s/m)
0.004	0.012	54.7	17.2	63

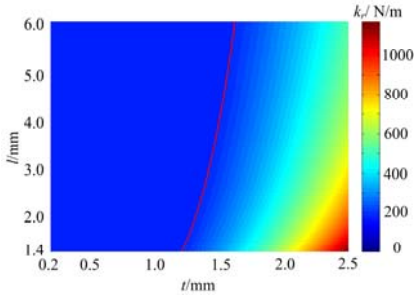

Fig.7. The rotational stiffness of the flexure hinge.

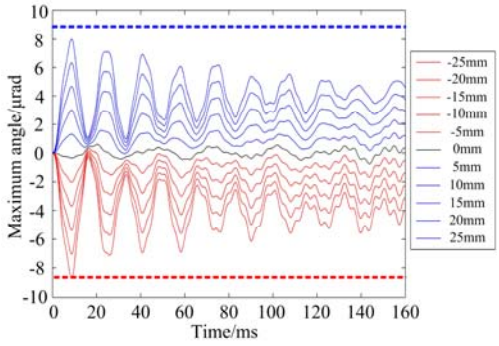

Fig.8. The angular displacements of the working table at different initial positions.

V. EXPERIMENTS

The XY stage has been manufactured, and it is shown in Fig.9, where Parker 310-4N-NC-WD3S-X linear motors, Aries-13-A-E driver and RENISHAW RGH22 grating encoder were used.

The open-loop dynamic characteristics of the stage were investigated, and the experimental setup is shown in Fig.10, where excitation forces were generated by a hammer, and the response signals were collected by a BK4368 acceleration sensor and amplified by a BK2692 amplifier. TJDAS dynamic measurement system was used to collect the excitation forces and the response signals. The transfer function is depicted in Fig.11, and the result shows the vibrations occurs at 209 and 453 Hz.

Experiments were carried out to examine the performance of the XY stage with a PID controller which was realized by a Turbo PMAC2 motion control card. A RENISHAW EC10/ML10 laser interferometer was used for the dynamic position measurements. The environmental factors were tested firstly, and the result shows the displacement noise amplitude was less than ±15 nm.

The step responses with reference displacements of ±25 mm were investigated, and the displacement and velocity are summarized in Fig.12. The X-axis setting time was 112 ms, steady state error was 0.5 μm, and velocity could reach up to 0.59 m/s. The Y-axis setting time was 124ms, steady state error was 0.5 μm, and velocity could reach 0.62 m/s.

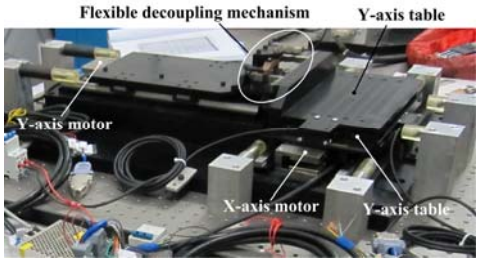

Fig.9. The XY micropositioning stage.

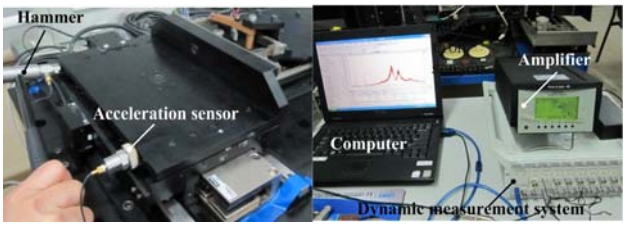

Fig.10. The experimental setup for dynamic characteristic investigation.

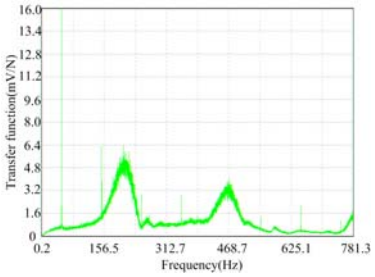

Fig.11. The open–loop dynamic test result.

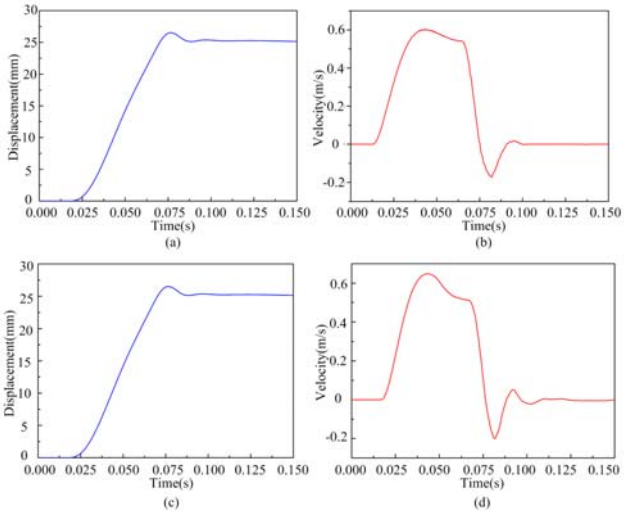

Fig.12. The step responses with reference displacement of ±25 mm: (a) X-axis displacement, (b) X-axis velocity t, (c) Y-axis displacemen, and (d) Y-axis velocitv.

The rotation of the XY stage was investigated, and the measurement method is shown in Fig.13. Motion ranges of ±25 mm were divided into 10 segments in X- and Y-axes, respectively. The displacement of each point was measured by

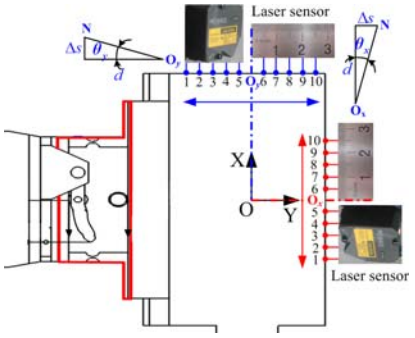

Fig. 13. The measurement method of XY stage rotation.

TABLE II
THE ROTATION ANGLES OF THE XY STAGE(°)

Points	1	2	3	4	5
X-axis	0.45	0.34	0.32	0.21	0.09
Y-axis	0.42	0.36	0.23	0.15	0.10
Points	6	7	8	9	10
X-axis	0.12	0.25	0.32	0.36	0.47
Y-axis	0.08	0.12	0.27	0.34	0.41

laser displacement sensors and the rotation angles of the stage were calculated. The points of O_x and O_y were selected as the X- and Y-axes reference points, respectively. For each point, the displacement was measured for five times, and the average displacements were used for calculate the rotation angles. The results were summarized in Table 2, and it can be found the rotation angles were within 0.5˚.

Motion range of ±25 mm was divided into 10 segments by 11 points. When the table moved with a step size of 5 mm, laser interferometer measured the displacement errors of each point, and three motion cycles were operated, and thus six displacement errors were recorded in all at every point. Thus, the positioning accuracy and repeatability of the XY stage can be obtained and shown in Fig.14. The results show that X-axis positioning accuracy was 0.6 μm, and the repeatability was 0.3 μm. Y-axis positioning accuracy was 0.5 μm, and the repeatability was 0.3 μm.

Actual positioning experiments for microelectronic thermosonic bonding were carried out with the aid of a vision system [27], and the experimental results show that the positioning with sub-micrometer accuracy within large motion strokes can be accomplished.

VI. CONCLUSION

This paper presents a novel flexure-based kinematically decoupled XY positioning stage directly driven by two linear motors. The mechanism of the XY positioning stage has been introduced firstly, and the dynamic model of the XY stage has been established. Dynamic design has been carried out, and the result shows that the rotational stiffness of the flexure hinges should be larger than 180 N/m to ensure that the angular displacement of working table was within ±0.5° with the motion stroke form -25 mm to 25 mm. Finally the geometric parameters of the flexure hinges were determined. The stage performance was investigated, and the results show that there are vibrations at 209 and 453 Hz. When the reference displacement was 25 mm, X-axis setting time was 112 ms, steady state error was 0.5 μm and velocity could reach 0.59 m/s. Y-axis setting time was 124 ms, steady state error was 0.5 μm and velocity could reach 0.62 m/s. The angular displacements of the working table were less than ±0.5° within the ±25 mm motion stroke. X-axis positioning accuracy was 0.6μm and the repeatability was 0.3μm. Y-axis positioning accuracy and repeatability were 0.5μm and 0.3μm, respectively. Sub-micrometer accuracy positioning within large motion stroke can be accomplished using the developed stage. Compared with the traditional motor driven stages, the developed stages can provide higher positioning accuracy and speed. Compared with the PZT and voice coil motor actuated stages, the developed stage can provide larger motion stroke, and it is easy to increase the motion stroke through increasing the guide length. Because there are frictions and motion gaps between the guides and sliders, higher accuracy is difficult to achieve, so future work can be focused on designing novel air-supported stages to improve the positioning accuracy. And we can also carry out some work on the dynamic design and control methodologies of these kinds of high speed positioning stages [28]-[29].

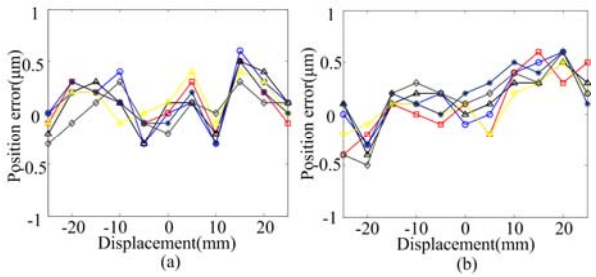

Fig. 14. Positioning accuracy: (a) X-axis and (b) Y-axis.

REFERENCES

[1] Y.M. Li, and Q.S Xu, "Design and robust repetitive control of a new parallel-kinematic xy piezostage for micro/nanomanipulation," *IEEE/ASME Transactions on Mechatronics*, vol. 17, no. 6, pp. 1120-1132, 2012.

[2] F. Wang, C. Liang, Y. Tian, X. Zhao, and D. Zhang, "Design of a piezoelectric-actuated microgripper with a three-stage flexure-based amplification," *IEEE/ASME Transactions on Mechatronics*, vol. 20, no. 5, pp. 2205-2213, Oct. 2015..

[3] Q.S. Xu, "Design and development of a compact flexure-based xy precision positioning system with centimeter range," *IEEE Transactions on Industrial Electronics*, vol. 61, no. 2, pp. 893-903, 2014.

[4] Y. Tian, B. Shirinzadeh, D. Zhang, and G. Alici, "Development and dynamic modelling of a flexure-based Scott–Russell mechanism for nano-manipulation", *Mechanical Systems and Signal Processing*, vol. 23, no. 3, pp. 957-978, 2009.

[5] F. Wang, Z. Ma, W. Gao, X. Zhao, Y. Tian, D. Zhang, and C. Liang. "Dynamic modeling and control of a novel XY positioning stage for semiconductor packaging," *Transactions of the Institute of Measurement and Control*, vol. 37, no. 2, pp. 1107-1120, 2015.

[6] S. Xiao and Y. M. Li, "Optimal design, fabrication and control of an XY micro-positioning stage driven by electromagnetic actuators," *IEEE*

Transactions on Industrial Electronics, vol. 60, no.10, pp.4613-4626, 2013.

[7] H. Tang and Y. M. Li, "A new flexure-based yθ nanomanipulator with nanometer scale positioning resolution and millimeter range workspace," *IEEE/ASME Transactions on Mechatronics*, vol. 20, no. 3, pp. 1320-1330, June 2015.

[8] F. Wang, X. Zhao, D. Zhang, Z. Ma, and X. Jing, "Robust and precision control for a directly-driven XY table," *Proceedings of the Institution of Mechanical Engineers, Part C: Journal of Mechanical Engineering Science*, vol. 225, pp. 1107-1120, 2011.

[9] M. Moallem, and V. A.Tabrizi, "Tracking control of an antagonistic shape memory alloy actuator pair," *IEEE Transactions on Control Systems Technology*, vol. 17, no. 1, pp. 1107-1120, 2009.

[10] L. Riccardi, D. Naso, B. Turchiano, and H. Janocha, "Adaptive control of positioning systems with hysteresis based on magnetic shape memory alloys," *IEEE Transactions on Control Systems Technology*, vol. 21, no. 6, pp. 2011-2023, 2013.

[11] K. Liang, K. Kao, and S. Tien, "Precision positioning with shape-memory-alloy actuators," *International Journal of Automation and Smart Technology*, vol. 3, no. 4, pp. 265-271, 2013.

[12] L. Riccardi, D. Naso, H. Janocha, and B. Turchiano, "A precise positioning actuator based on feedback-controlled magnetic shape memory alloys," *Mechatronics*, vol. 22, no. 5, pp. 568-576, 2012.

[13] M.R. Zakerzadeh, and H. Sayyaadi, "Precise position control of shape memory alloy actuator using inverse hysteresis model and model reference adaptive control system," *Mechatronics*, vol. 23, no. 8, pp. 1150-1162, 2013.

[14] Y.M. Li, and Q.S. Xu, "Design and robust repetitive control of a new parallel-kinematic XY piezostage for micro/nanomanipulation," *IEEE/ASME Transactions on Mechatronics*, vol.17, no.6, pp.1120-1132, 2012.

[15] G.Y. Gu, and L.M. Zhu, "High-speed tracking control of piezoelectric actuators using an ellipse-based hysteresis model," *Review of Scientific Instruments*, vol.81, no.8, pp.085104, 2010.

[16] Y.M. Li, and Q.S. Xu, "Development and assessment of a novel decoupled XY parallel micropositioning platform," *IEEE/ASME Transactions on Mechatronics*, vol. 15, no. 1, pp. 125-135, 2010.

[17] J. Dong, Q. Yao, and P. Ferreira, "A novel parallel-kinematics mechanisms for integrated, multi-axis nanopositioning Part 2: Dynamics, control and performance analysis," *Precision Engineering*, vol. 32, pp. 20-33, 2008.

[18] Q. Yao, J. Dong, and P. Ferreira, "A novel parallel-kinematics mechanisms for integrated, multi-axis nanopositioning Part 1. Kinematics and design for fabrication," *Precision Engineering*, vol. 32, pp. 7-19, 2008.

[19] Y. Qin, B. Shirinzadeh, Y. Tian, D. Zhang, and U. Bhagat, "Design and computational optimization of a decoupled 2-DOF monolithic mechanism," *IEEE/ASME Transactions on Mechatronics*, vol. 19, no. 3, pp. 872-881, 2014.

[20] G.Y. Gu, L.M. Zhu, C.Y. Su, and H. Ding, "Motion control of piezoelectric positioning stages: modeling, controller design, and experimental evaluation," *IEEE/ASME Transactions on Mechatronics*, vol. 18, no. 5, pp. 1459-1471, 2013.

[21] Y. Qin, Y. Tian, D. Zhang, B. Shirinzadeh, and S. Fatikow, A novel direct inverse modeling approach for hysteresis compensation of piezoelectric actuator in feedforward applications. *IEEE/ASME Transactions on Mechatronics*, Vol. 18, No. 3, pp. 981-989, 2013.

[22] J. Xu, D. Huang, V. Venkatakrishnan, and T. Huynh, "Extreme precise motion tracking of piezoelectric positioning stage using sampled-data iterative learning control," *IEEE Transactions on Control Systems Technology*, vol. 21, no. 4, pp. 1432-1439, 2013.

[23] S. Xiao and Y.M. Li, "Modeling and high dynamic compensating the rate-dependent hysteresis of piezoelectric actuators via a novel modified inverse Preisach model", *IEEE Transactions on Control Systems Technology*, vol. 21, no. 5, pp.1549-1557, 2013.

[24] C. Lin, H. Yau, and Y. Tian, "Identification and compensation of nonlinear friction characteristics and precision control for a linear motor stage," *IEEE/ASME Transactions on Mechatronics*, vol. 18, no. 4, pp. 1385-1396, 2013.

[25] Y. Tian, B. Shirinzadeh, D. Zhang, and Y. Zhong, "Three flexure hinges for compliant mechanism designs based on dimensionless graph analysis," *Precision Engineering*, vol. 34, no. 1, pp.92-100, 2010.

[26] S.W. Liu, "Vision positioning method and system development for wire bonder," M.S. dissertation, Dept. Mech. Eng., Univ. Tianjin, Tianjin, 2011.

[27] F. Wang, J. Li, S. Liu, X. Zhao, D. Zhang, and Y. Tian, "An improved adaptive genetic algorithm for image segmentation and vision alignment used in microelectronic bonding," *IEEE/ASME Trans. Mechatronics*, vol.19, no.3, 916-923, 2014.

[28] G. Gu, L. Zhu, C. Su, H. Ding, and S. Fatikow, "Proxy-based sliding mode tracking control of piezoelectric-actuated nanopositioning stages," *IEEE/ASME Transactions on Mechatronics*, vol. 20, no. 4, pp. 1956-1965, Aug. 2015.

[29] G. Gu, L. Zhu, C. Su, H. Ding, and S. Fatikow, "Modeling and control of piezo-actuated nanopositioning stages: A survey," *IEEE Transactions on Automation Science and Engineering*, DOI: 10.1109/TASE.2014.2352364.